Quantum Electronics **51** (11) 992–999 (2021)

CONTROL OF LASER RADIATION PARAMETERS https://doi.org/10.1070/QEL17641

Investigation of spatial and temporal characteristics of turbulent-distorted laser radiation during its dynamic phase correction in an adaptive optical system

V.N. Belousov, V.A. Bogachev, M.V. Volkov, S.G. Garanin, A.V. Kudryashov, A.N. Nikitin, A.L. Rukosuev, F.A. Starikov, Yu.V. Sheldakova, R.A. Shnyagin

Abstract. **We report the results of the analysis of experiments on dynamic phase correction of laser radiation distorted by a turbulent airflow in an adaptive optical system (AOS) with a Shack–Hartmann wavefront sensor (WFS). A field-programmable gate array is used as the main AOS control element, which provides a closed loop AOS bandwidth of up to 2000 Hz. The WFS is used to estimate the characteristic bandwidth of the generated turbulence ν_{turb}. Changes in the spatial and temporal spectra of the laser radiation phase, as well as the quality of the beam during its dynamic phase correction at various AOS frequencies, are analysed. It is shown experimentally and by calculation that to ensure a high efficiency of the wavefront correction, the AOS frequency should be at least 20 times higher than ν_{turb}.**

Keywords: *adaptive optics, wavefront sensor, field-programmable gate array, atmospheric turbulence.*

1. Introduction

The problem of transporting laser radiation under the conditions of the Earth's atmosphere is relevant for energy transfer and laser communication (see, e.g., [1–4]). One of the significant limitations on the energy transfer efficiency is the change in the local refractive index in turbulent airflows, because of which the wavefront of laser radiation propagating through the atmosphere acquires dynamic spatial distortions [5]. These distortions reduce the quality of focusing. As a result, the efficiency of laser energy transmission is reduced up to the complete loss of system functionality.

Correction of the laser radiation wavefront in an adaptive optical system (AOS) in real time reduces the effect of turbulence. Effective phase correction in this regime requires a corresponding response speed of the AOS. As shown in [6], the characteristic spectrum of atmospheric fluctuations reaches frequencies of ~100 Hz and higher. According to simple estimates [7], the AOS operating speed should be at least an order of magnitude greater than this value, i.e., be at least 1000 Hz. When using a conventional personal computer (PC) to control the AOS, it is difficult to achieve such a high operation speed due to delays in the operating system or a number of difficulties in organising parallel computations.

One of the ways to solve the problem of increasing the AOS speed is to use a programmable logic device (PLD) in the control system instead of a PC. The authors of [8, 9] reported on the creation of a fundamentally new AOS using a field-programmable gate array (FPGA) – a type of a PLD [10] – as the main control element. The frequency bandwidth of the AOS operating with the Shack–Hartmann wavefront sensor (WFS) [11–13] reached as high as 2000 Hz in a closed-loop cycle.

The present work was aimed at a detailed computational and experimental study of the spatial and temporal characteristics of laser radiation upon its dynamic phase correction in the AOS, depending on its response speed, as well to revealing the conditions for efficient correction. The research tool was an FPGA-based AOS [8].

2. Adaptive optical system

A schematic of the AOS is shown in Fig.1. A plane-parallel laser beam 50 mm in diameter with the intensity distribution shown in Fig. 2 is formed using collimating lens *2* from the radiation of a 1 mW diode laser (*1*) coupled to an optical fibre. The radiation wavelength of 0.65 μm was chosen to facilitate visual alignment of the AOS; radiation with a different wavelength corresponding to the spectral sensitivity of the WFS camera can be also used. Dynamic distortions of the wavefront were produced using a 1.5 kW fan heater with an outlet diameter of 130 mm, the air flow of which was directed to the laser beam perpendicular to its axis after passing through collimating lens *2* with a focal length of 300 mm. Then the distorted laser beam hits the bimorph-type adaptive mirror (AM) *3* [14–16] and is reflected from it in the direction of a possible consumer (*4*). The distance from the collimating lens to the mirror was 1300 mm. A small part of the laser beam is diverted to a WFS (*5*) using a beam splitter (*6*) (the optical path length from the mirror to the WFS is 2660 mm). The video information from the WFS camera enters a FPGA (*7*), which processes this information, calculating the voltage vector based on the preloaded coordinates of the focal points of the reference wavefront and the mirror response functions.

V.N. Belousov, A.N. Nikitin, A.L. Rukosuev, Yu.V. Sheldakova Institute of Geosphere Dynamics, Russian Academy of Sciences, Leninsky prosp. 38, korpus 1, 119334 Moscow, Russia; e-mail: alru@nightn.ru;
V.A. Bogachev, M.V. Volkov, S.G. Garanin, F.A. Starikov, R.A. Shnyagin Institute of Laser Physics Research, Russian Federal Nuclear Centre – All-Russian Scientific Research Institute of Experimental Physics (RFNC-VNIIEF), prosp. Mira 37, 607188 Sarov, Nizhny Novgorod region, Russia;
A.V. Kudryashov Institute of Geosphere Dynamics, Russian Academy of Sciences, Leninsky prosp. 38, korpus 1, 119334 Moscow, Russia; Moscow Polytechnic University, ul. B. Semenovskaya 38, 107023 Moscow, Russia

Received 29 June 2021; revision received 7 October 2021
Kvantovaya Elektronika **51** (11) 992–999 (2021)
Translated by V.L. Derbov

These voltages are transmitted to an AM control unit (CU) (*8*), which converts the digital code of voltages into an analogue signal and amplifies it to the value determined by the AM parameters. Then the generated voltages are applied to the mirror electrodes to correct wavefront distortion. A personal computer (*9*) in this scheme is not included in the operational control circuit of the AOS. It serves to set the required AOS operation regime, load the reference coordinates of the focal points, load the response functions of the AM, and also obtain information from the FPGA about the correction process for subsequent postprocessor analysis.

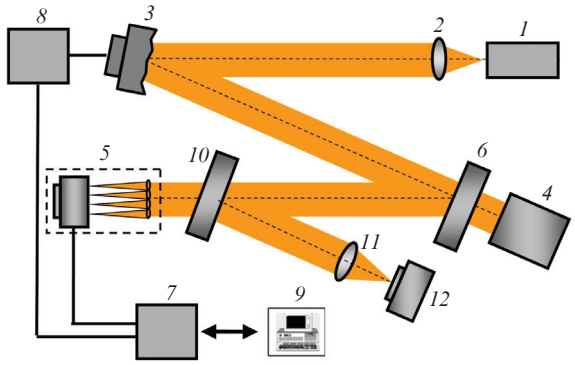

Figure 1. Schematic of the adaptive optical system: (*1*) laser; (*2*, *11*) lens; (*3*) adaptive mirror; (*4*) consumer; (*5*) WFS; (*6*, *10*) beam splitter; (*7*) FPGA; (*8*) control unit; (*9*) PC; (*12*) CMOS camera.

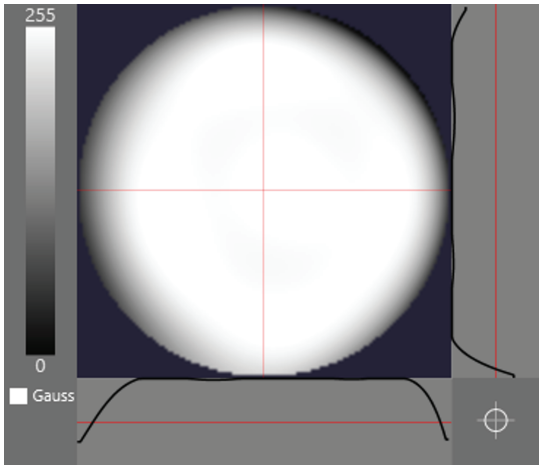

Figure 2. Distribution of laser radiation intensity at the collimator output.

To register the wavefront in the AOS, a Shack–Hartmann WFS is used [17, 18]. The AOS implements the phase conjugation algorithm, in which the wavefront of the output radiation should tend to a given reference wavefront, in particular, to a flat one. The closed loop control was implemented according to the proportional algorithm. With effective dynamic phase correction of the laser beam, the AOS forms a flat wavefront at the exit due to the retention of the hartmannogram spots in time in the reference positions.

The main tasks that the FPGA solves in this configuration are to obtain video information from the WFS, to process the WFS information (calculating the coordinates of focal points and calculating the voltage vector for the AM), to send a digital representation of the voltage vector to the control unit, and to exchange information with the PC. Compared to PCs, FPGAs provide faster computations due to their hardware implementation and parallelisation of computation processes. In addition, the FPGA has a low-level access to the camera and control equipment, which allows work with data streams to be optimised, thereby reducing the wavefront correction cycle time.

The parameters of the Shack–Hartmann WFS, implemented on the basis of a JetCam-19 high-speed camera and a Kaya Komodo Frame Grabber (Kaya Instruments) [19], are presented below.

Kaya JetCam-19 camera	
Spectral range/nm	350–1100
Dynamic range	$\pm 50\lambda$
Measurement accuracy/PV	$\lambda/15$
Kaya Komodo Frame Grabber	
Frame rate/fps:	
resolution 1920 × 1080 pixels	2400
resolution 480 × 480 pixels	4000
Interface	fibre, 40 Gb s^{-1}
Focal length	
of the lens array/mm	12
Number of operating	
subapertures	20 × 20
Maximum input beam size/mm	4.8 × 4.8
Resolution/bit	8
Weight/g	1260

The frame grabber card incorporates an Arria V GZ FPGA. All the electrical connections required to interface the camera and the FPGA have already been completed, and the corresponding software was developed and loaded into the FPGA to implement the closed-loop AOS algorithm. To connect the FPGA with external devices, additional I/O interfaces with the control unit and PC are implemented using SFP (small form-factor pluggable) expansion modules, the corresponding connectors for which are included in the frame grabber. The internal structure of the FPGA is shown in Fig. 3.

In addition to using fast computational algorithms, the implementation of the FPGA-based AOS control makes it possible to optimise the sequence of computations. The FPGA uses the WFS camera interface at the hardware level, which makes it possible to work with individual pixels in the process of their arrival at the frame grabber card, i.e. in real time. Having received several lines of the image containing the first row of focal points of the WFS hartmannogram, it is possible to calculate the coordinates of these points and fill in the corresponding elements of the matrix intended for calculating the voltage vector. Taking into account the fact that the bottom lines of the image as a rule do not contain useful information, immediately after obtaining the entire image, the vector of control voltages is calculated. The total time of one cycle is reduced to 0.5 ms, which corresponds to a frequency of 2000 Hz. The diagram of the time cycle of a closed AOS is shown in Fig. 4.

In the experiment, a bimorph DM2-50-31 AM was used to correct wavefront distortions, for which the configuration of the electrodes is shown in Fig. 5, and its parameters are presented below:

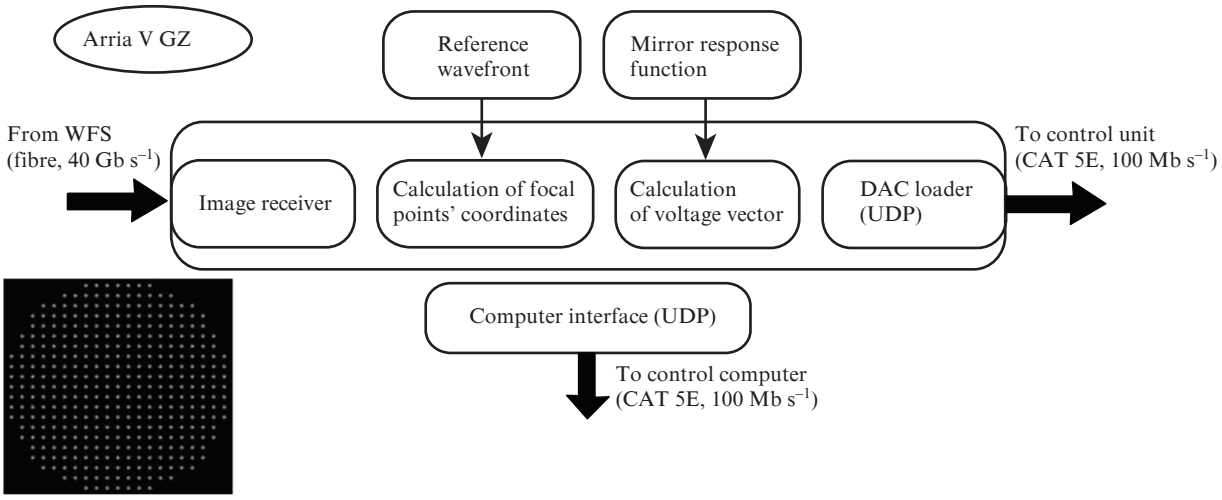

Figure 3. Internal structure of FPGA.

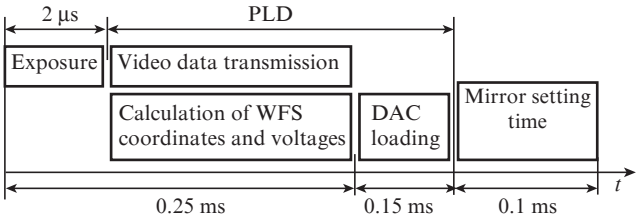

Figure 4. Timing diagram of one cycle of FPGA operation.

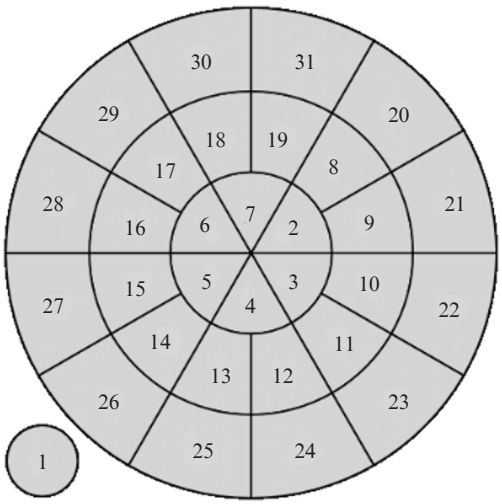

Figure 5. Configuration of electrodes of the bimorph adaptive mirror.

Clear aperture/mm	50
Number of control channels	31
Electrode ring width/mm	8
Deflection of the first electrode/μm	12
Deflection of the remaining electrodes/μm	2
First resonance frequency/kHz	8.3
Control voltage range/V	−200 ÷ +300

The first electrode, conventionally shown in the lower left corner of Fig. 5, is a full-aperture disk and is used to control the overall defocusing.

For an independent verification of the correction quality, the experimental setup contains a far-field indicator formed by lens *11* (see Fig. 1) with a focal length of 1 m and a Gig-E DMK23GM021 camera *12* [20] with a pixel size of 3.75 μm, located in the focal plane of the lens. The diffraction-limited diameter of the focal spot at a wavelength of 0.65 μm is 31.7 μm or 8.46 pixels.

3. Parameters of a laser beam with turbulent phase distortions

In the experiments [8], optical inhomogeneities along the laser beam propagation path were produced by a turbulent flow of heated air from a fan heater directed across the laser beam. It can be assumed that the duration of the existence of thermal inhomogeneities in the air is much longer than the time during which these inhomogeneities move under the influence of the wind within the beam aperture. This approximation is known in the literature as the Taylor hypothesis [21]. Within the framework of this hypothesis, the spatial scale of phase distortions is related to their time scale in such a way that the larger the distortions, the slower they are, and vice versa [5].

The angular divergence of the laser beam before correction is determined by the depth and scale of spatial phase distortions acquired in a turbulent medium. Figure 6 shows the instantaneous and 10-s averaged experimental distributions of the intensity of the laser beam on the matrix of the far-field camera, as well as the fraction of the radiation power in the angle θ. The beam divergence at a 50% power level was $3.5\theta_d$, where θ_d is the diffraction divergence by the same criterion. The spatial scale of turbulent phase distortions is characterised by the Fried parameter r_0 [22], which can be determined using the Shack–Hartmann WFS from the phase gradients [23]. The value of the Fried parameter, determined using the WFS with an averaging time of 10 s, was approximately 1 cm, which qualitatively agrees with the estimate from the divergence (see Fig. 6). In this case, with a characteristic size of the mirror electrode of ~0.8 cm and the size of the WFS subaperture $s = 0.25$ cm (taking the scaling into account), the required spatial resolution of the AOS is provided [24].

Let us now consider the time scale of phase inhomogeneities in the experiment and the required time resolution of the

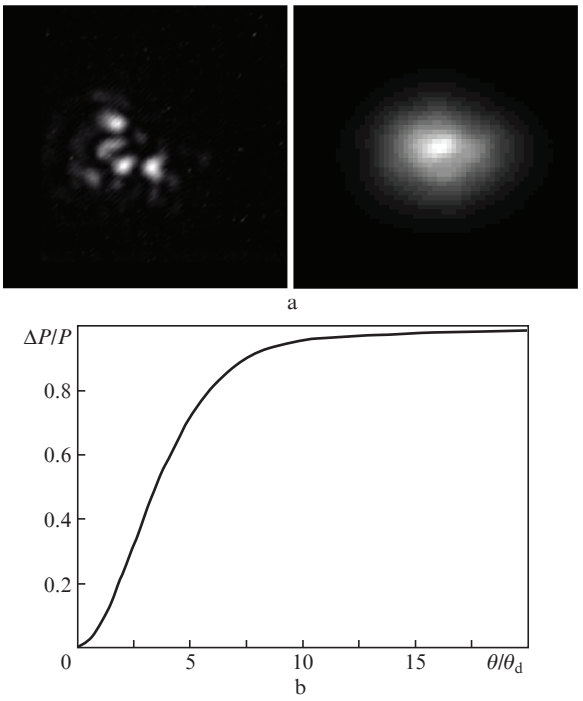

Figure 6. (a) Instantaneous and average distributions of the laser beam intensity in the far-field zone and (b) fraction of the power P of the laser radiation in the angle θ.

AOS. Knowing the dynamics of all centroids of the WFS hartmannogram relative to the reference points, it is possible to reconstruct the wavefront dynamics. In the present work, when reconstructing the laser beam wavefront, we used the Fried sampling scheme and the method described in Ref. [25]. In this scheme, the gradient values are measured at the centre of the square cell where the phase values are to be determined. When the number of WFS subapertures is $N \times N$, the phase of the laser beam is determined on a grid with dimensions $(N + 1) \times (N + 1)$. Figure 7 shows a typical experimental hartmannogram at $s = 0.25$ cm ($N = 20$), and Fig. 8 shows the phase distributions with an interval of 6.67 ms (the operation rate of the WFS in these experiments on measuring the dynamics of the wavefront is 1 kHz). It can be seen from Fig. 8 that the change in the phase pattern in time is predominantly of a shear nature, determined by the wind 'drift' of the phase. This is the nature of the change in the wavefront that is observed when the Taylor hypothesis is fulfilled (see, e.g., [26]). From the analysis of the displacement of the minima and maxima of the phase picture in time, the wind velocity v in the experiment was determined, which amounted to 0.8 m s^{-1} (0.74 and 0.3 m s^{-1} along the x and y axes, respectively). The dynamics of the local phase was obtained from the series of experimental wavefronts reconstructed at $s = 0.25$ cm (Fig. 8). Figure 9a shows the time power spectrum of the local phase fluctuations, averaged over the aperture [27]. For Kolmogorov turbulence, the phase spectrum is characterised by a power-law dependence on frequency with an exponent of –8/3 [28] (straight line in Fig. 9a). It can be seen that the generated turbulence in the frequency range of 10–200 Hz has a character close to Kolmogorov's one. Figure 9b shows the normalised integral of the phase power spectrum, i.e., the 'energy' of turbulence. Spectral 'energy' reaches 95% at a frequency of about 30 Hz.

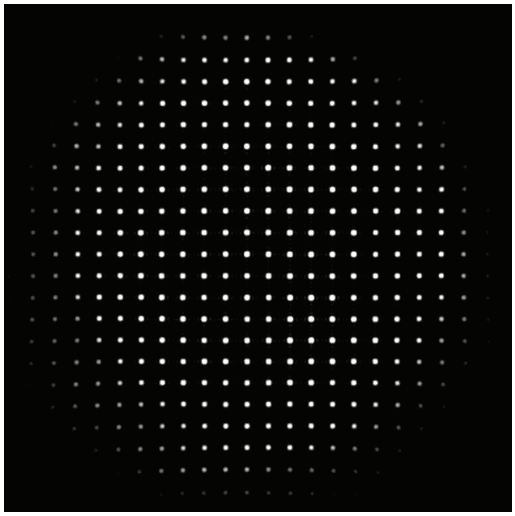

Figure 7. Typical WFS hartmannogram at $s = 0.25$ cm.

A certain conclusion about the bandwidth of significant turbulent distortions can be drawn from a simple analysis of the dynamics of the hartmannogram centroids [8, 26]. Figure 10 shows the experimentally obtained dynamics of centroid fluctuations in the WFS subaperture at $s = 0.25$ cm along the horizontal x axis (due to the different wind speeds along the x and y axes, the frequency of centroid fluctuations along the y-axis is somewhat lower). Due to the statistical homogeneity of the wavefront over the beam aperture, the dynamics of centroid fluctuations in all subapertures, except for the boundary ones, is approximately the same.

A series of experimental wavefronts reconstructed at $s = 0.25$ cm makes it possible to obtain a series of hartmannograms with an increased subaperture size s and to compare the dynamics of centroid fluctuations on WFS subapertures of different sizes.

Figure 11a shows the power spectrum of centroid fluctuations (taking into account the total fluctuations along the x and y axes), and Fig. 11b presents the normalised integral of the power spectrum, i.e., the spectral 'energy', at $s = 0.25$, 0.7 and 1 cm for the wavefront in the absence of correction. As can be seen from Fig. 11a, the amplitude of centroid fluctuations decreases with increasing size of the WFS subaperture. With an increase in the subaperture, the frequency at which the integral of the power spectrum becomes saturated also decreases – the minimum scale of the recorded phase inhomogeneities of the turbulent medium, which contribute to the centroid fluctuations, increases.

If we characterise the turbulence bandwidth ν_{turb} by the level of 95% of the spectral energy of centroid fluctuations at the WFS subaperture [26], then, as can be seen from Fig. 11b, $\nu_{\text{turb}} = 60$, 30, and 25 Hz for s = 0.25, 0.7, and 1 cm, respectively. The turbulence bandwidth determined in this way carries no information about the size and amplitude of phase distortions over the entire beam aperture. The minimum spatial scale of phase inhomogeneities that contribute to the divergence of the laser beam is determined by the Fried parameter. Therefore, in order to track all scales of phase inhomogeneities that require correction, the size of the WFS subaperture s must be close to the Fried parameter [26]. In our case, $r_0 = 1$ cm. For $s = 1$ cm, the turbulence bandwidth to be corrected is $\nu_{\text{turb}} \approx 25$ Hz.

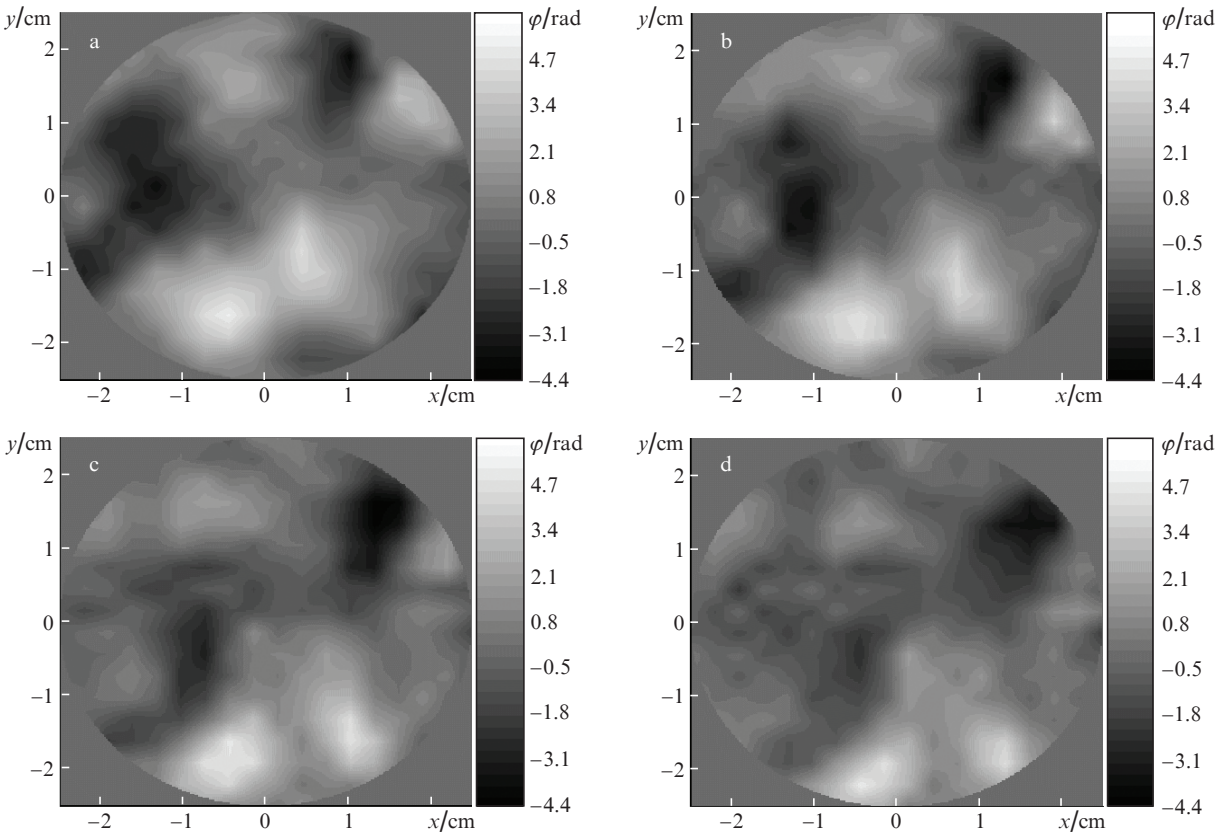

Figure 8. Experimental laser radiation phase distributions with a step of 6.67 ms at $s = 0.25$ cm.

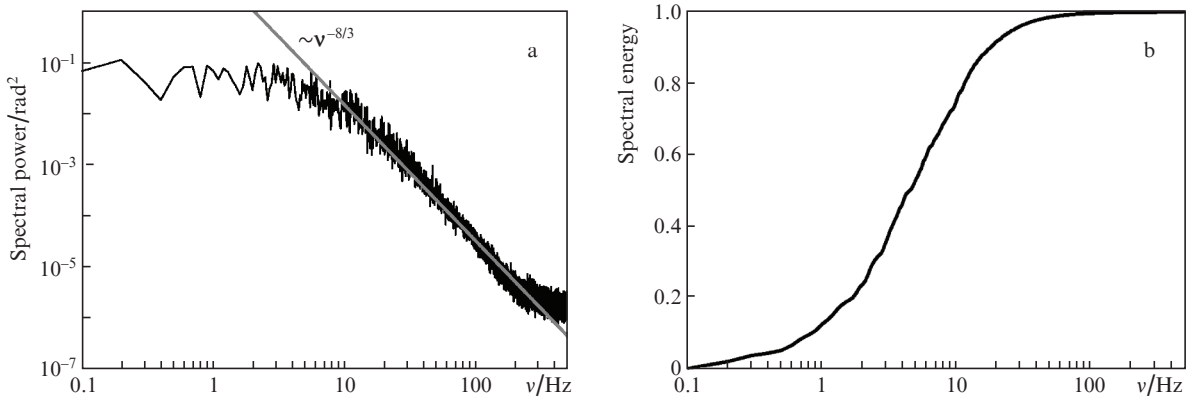

Figure 9. (a) Average power spectrum of phase fluctuations (grey straight line – dependence $\sim\nu^{-8/3}$) and (b) normalised integral of the phase power spectrum.

Thus, the formed turbulence leads to the following spatial and temporal characteristics of the laser radiation phase: $r_0 = 1$ cm and $\nu_{\text{turb}} = 25$ Hz. According to the results of calculations [26], the required operating frequency of the AOS (ν_{AOS}) for efficient compensation of turbulence with the Strehl number reaching 0.7–0.8 should exceed ν_{turb} by a factor of 20, i.e., it should be about 500 Hz. It is interesting to compare the estimated frequency ν_{AOS} with the classical parameters of Kolmogorov turbulence, based on which the requirements for the speed of atmospheric AOS are determined – the Greenwood frequency $\nu_{\text{G}} = 0.427v/r_0$ [29] and the inverse coherence time $1/\tau_0 = \nu_{\text{G}}/0.134$ [30]. At a wind speed of 0.8 m s^{-1}, we have $\nu_{\text{G}} = 34$ Hz, $1/\tau_0 = 254$ Hz, i.e., the Greenwood frequency is close to ν_{turb} and, according to [26], $1/\tau_0$ is half the required frequency of the AOS operation.

4. Results of laser beam wavefront correction and their analysis

We investigated the efficiency of phase correction of a laser beam with turbulent phase disturbances at various AOS operating frequencies up to $\nu_{\text{AOS}} = 2000$ Hz. The change in ν_{AOS} towards a decrease was implemented by introducing a time delay after the transfer of control voltages to the con-

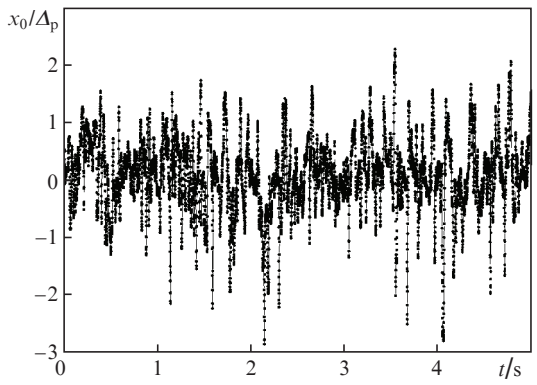

Figure 10. Experimental dynamics of the ratio of the centroid deviation x_0 in the WFS subaperture along the x axis to the WFS camera pixel size Λ_p at $s = 0.25$ cm.

trol unit (see Fig. 4), and the exposure time remained unchanged.

Figure 12 shows the temporal spectra of centroid fluctuations and the dependence of the time-averaged magnitude of the coefficient A_{N_Z} of the laser beam wavefront expansion in Zernike polynomials on the polynomial number N_Z before and during the correction. The wavefront was reconstructed from the experimental dynamics of phase gradients at s = 0.25 cm. The AOS correction frequency in this experiment was 1500 Hz. The numbering of polynomials corresponds to the Noll indexing [31]. Lower harmonics correspond to lower N_Z values.

Phase correction leads to a decrease in the amplitude of spatial and temporal harmonics; the lower harmonics with a smaller frequency are corrected most intensively. This behaviour of the spatial and temporal spectra of phase distortions during correction in AOS with a finite speed is characteristic of Kolmogorov turbulence (see, e.g., [26]).

Figure 13 shows the instantaneous distributions of the laser radiation intensity in the far-field zone at different frequencies of the AOS correction, each distribution being normalised to its maximum intensity value. It can be seen that the quality of the focal spot improves with an increase in the correction frequency ν_{AOS}. The angular distributions of the laser radiation power at different correction frequencies are shown in Fig. 14.

The analysis of Figs 13 and 14 shows that with an increase in the phase correction frequency, the divergence decreases with the redistribution of the laser radiation energy in the far-

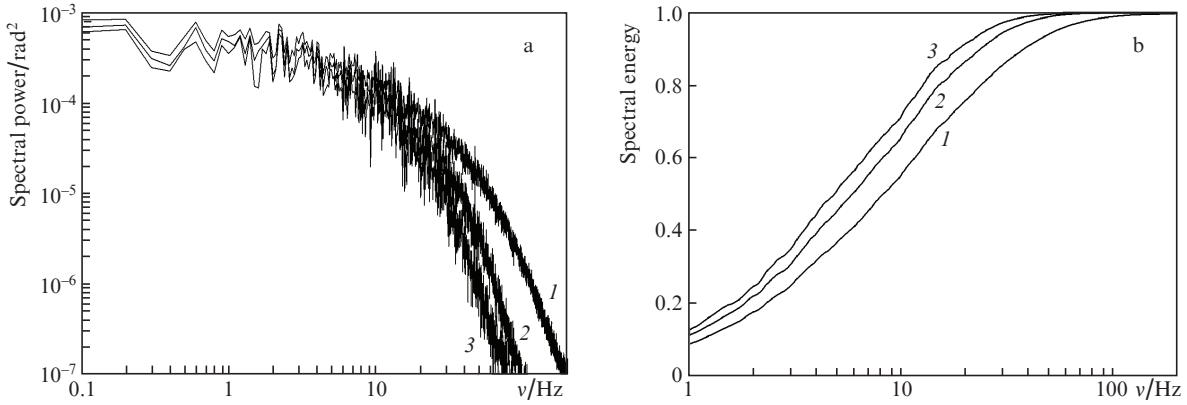

Figure 11. (a) Power spectra of centroid fluctuations in the WFS and (b) normalised integrals of the power spectrum at s = (*1*) 0.25, (*2*) 0.7 and (*3*) 1 cm.

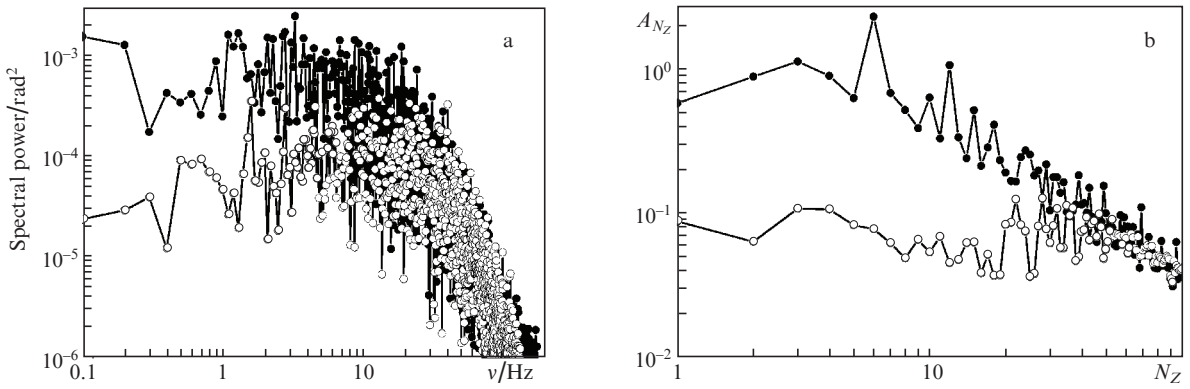

Figure 12. (a) Time spectra of fluctuations of the WFS centroid and (b) the dependence of the time-averaged magnitude of the coefficient A_{N_Z} in the laser beam wavefront expansion in Zernike polynomials on the polynomial number N_Z before correction (black circles) and during correction (white circles).

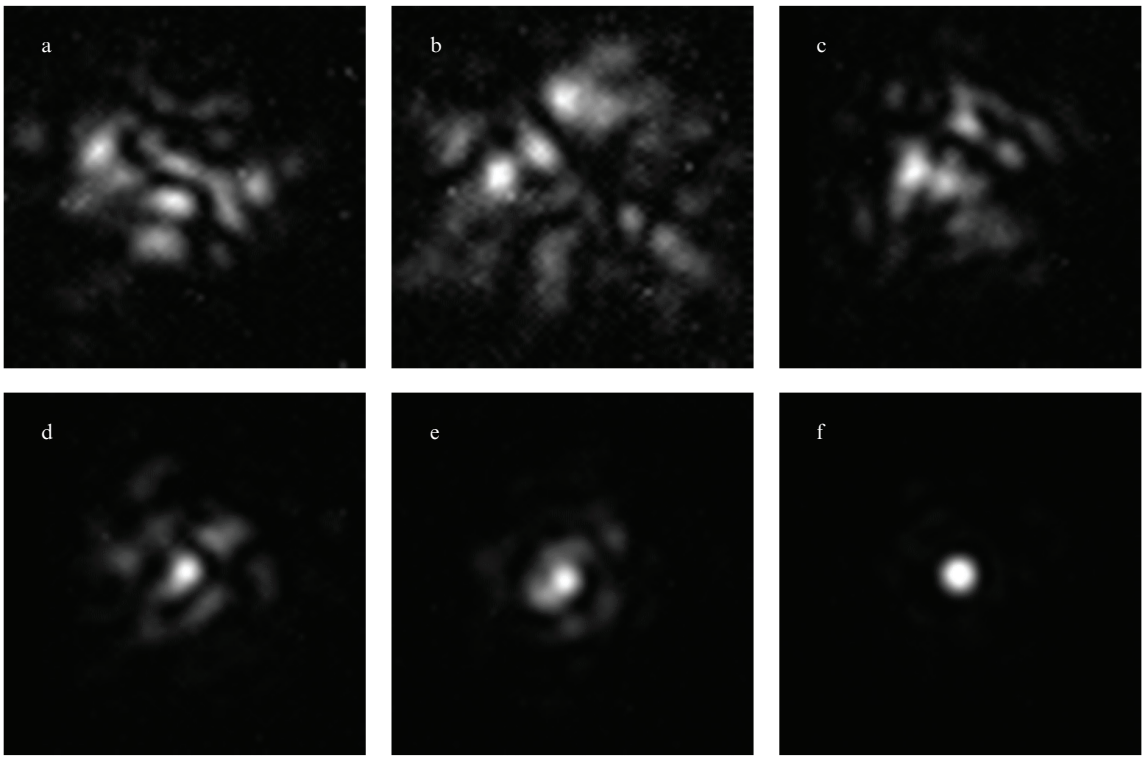

Figure 13. Instantaneous distributions of laser intensity in the far-field at AOS correction frequencies of (a) 10, (b) 25, (c) 100, (d) 200, (e), 500, and (f) 2000 Hz.

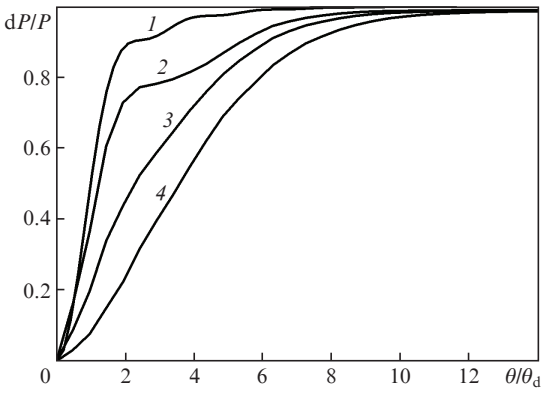

Figure 14. Fractions of laser radiation power P in the angle θ at (*1*) diffraction divergence and at ν_{AOS} = (*2*) 2000, (*3*) 200, and (*4*) 25 Hz.

field zone. Part of the energy from the 'wing' is transferred to the paraxial region, forming a narrowly directed core. When corrected at a frequency of 2000 Hz, the AOS provides a narrowly directed core in the far-field zone, which contains about 80% of the total laser radiation energy. The rest of the energy is contained in the wing, the presence of which is due to uncompensated small-scale (less than the spatial resolution of the AM) turbulent distortions.

A comparison of the results of experiments and numerical simulation of the AOS operation is illustrated in Fig. 15, which shows the dependence of the ratio of the actual laser radiation divergence to the diffraction divergence (θ/θ_d) on the ratio of the correction frequency ν_{AOS} to the turbulent distortion bandwidth ν_{turb} = 25 Hz. The computational model is described in Ref. [26]. The wavefront dynamics was reconstructed from the experimentally measured phase gradients. The phase correction was calculated in the approximation of an adaptive mirror with ideal spatial resolution. The solid horizontal line corresponds to the level of laser radiation divergence in the presence of turbulent phase distortions, and the dashed line corresponds to the minimum divergence (diffraction limit).

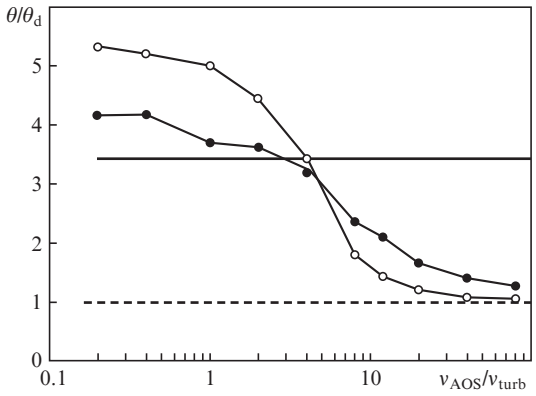

Figure 15. Dependences of the ratio of the laser radiation divergence to the diffraction divergence on the ν_{AOS}/ν_{turb} ratio at ν_{turb} = 25 Hz in the experiment (black circles) and calculation (white circles).

It is seen that the results of calculations simulating the operation of the AOS are in qualitative agreement with the experimental data. A certain quantitative discrepancy at high ν_{AOS} is caused by the fact that in the calculations the AM provided 'ideal' spatial resolution, while in experiments it was

finite. At low frequencies ν_{AOS}, the experimental divergence is lower than the calculated one, since in experiments, background subtraction in the far zone is accompanied by some loss of large-angle signal components.

Since the exposure time under these conditions is negligible, at low response rates, the operation of the AOS negatively affects the quality of the beam: The AOS introduces additional distortions into the laser beam, and the divergence of the laser radiation even increases relative to the initial level. A decrease in the radiation divergence with respect to the initial one is observed at $\nu_{AOS}/\nu_{turb} \geqslant 4$. As noted above, according to [26], in order to effectively compensate for turbulence when the Strehl ratio reaches 0.8, the required frequency ν_{AOS} must exceed ν_{turb} by a factor of 20, which is achieved at $\nu_{AOS} = 500$ Hz, and the calculations confirm this statement (see Fig. 15). The experiment, however, showed that at $\nu_{AOS}/\nu_{turb} = 20$, the beam quality has not yet reached its limit. A further increase in the AOS frequency (from 500 to 2000 Hz) leads to a decrease in θ/θ_d from 1.7 to 1.3 (cf. Figs 13e and 13f).

5. Conclusions

We have studied experimentally and numerically the spatial and temporal phase characteristics and quality of the radiation beam, distorted by a turbulent air flow under laboratory conditions, with its phase correction at different operating frequencies of the AOS. In the experiments, we have used an AOS with a bandwidth of up to 2000 Hz with a Shack–Hartmann WFS and a field-programmable gate array as the main control element.

The analysis of the time spectrum of the laser beam phase makes it possible to conclude that the turbulence character is close to Kolmogorov's one. With the Fried parameter $r_0 = 1$ cm, a good spatial resolution of the AOS is ensured. The turbulence bandwidth ν_{turb} determined at a level of 95% of the spectral energy of centroid fluctuations at the WFS subaperture corresponding to $r_0 = 1$ cm was 25 Hz. Earlier, it was confirmed by calculation [26] that to provide a highly efficient correction of the wavefront, the operating frequency of the AOS should be 20 times higher than ν_{turb}. In our case, this is achieved at $\nu_{AOS} = 500$ Hz (note that the Greenwood frequency is $\nu_G = 34$ Hz, the inverse coherence time is $1/\tau_0 = 254$ Hz). Nevertheless, a further increase in the response rate of the AOS to 2000 Hz leads to an additional decrease in the divergence from 1.7 to 1.3 of the diffraction limits.

Acknowledgements. This work was supported by Rosatom (Project EOTPLT-386) in the framework of the scientific programme of the National Centre for Physics and Mathematics.

References

1. Lu M., Bagheri M., James A.P., et al. *IEEE Access*, **6**, 29865 (2018).
2. Landis G.A., Westerlund L.H. *Laser Beamed Power – Satellite Demonstration Applications. NASA Contractor Report 190793*, IAF-92-0600, 18 (1992).
3. Huang Q., Liu D., Chen Y., et al. *Opt. Express*, **26**, 13536 (2018).
4. Vorontsov M., Weyrauch T., Carhart G., et al. *Lasers, Sources and Related Photonic Devices, OSA Technical Digest Series (CD)*, LSMA1 (2010); https://doi.org/10.1364/LSC.2010.LSMA1.
5. Tatarskii V.I. *Rasprostranenie voln v turbulentnoi atmosfere* (Wave Propagation in a Turbulent Atmosphere) (Moscow: Nauka, 1967).
6. Andrews L.C., Phillips R.L. *Laser Beam Propagation Through Random Media*, 2nd Ed. (Bellingham: SPIE Press, 2005).
7. Rukosuev A.L., Kudryashov A.V., Lylova A.N., et al. *Atmos. Oceanic Opt*., **28**, 381 (2015).
8. Rukosuev A.L., Belousov V.N., Nikitin A.V. et al. *Quantum Electron*., **50**, 707 (2020) [*Kvantovaya Elektron*., **50**, 707 (2020)].
9. Kudryashov A., Rukosuev A., Nikitin A., Galaktionov I., Sheldakova J. *Opt. Express*, **28**, 37546 (2020).
10. Kudryashov A.V., Rukosuev A.L., Samarkin V.V., et al. P*roc. SPIE*, **10772**, 107720V (2018).
11. Malacara D. *Optical Shop Testing*, 3rd Ed. (New Jersey: John Wiley & Sons, 2007).
12. Neal D.R. *Shack-Hartmann Sensor Engineered for Commercial Measurement Applications* (SPIE Press, 2004).
13. Southwell W.H. *J. Opt. Soc. Am*., **70**, 998 (1980).
14. Toporovskiy V., Kudryashov A., Samarkin V., Sheldakova J., Rukosuev A., Skvortsov A., Pshonkin D. *Appl. Opt*., **58**, 6019 (2019).
15. Cherezova T.Yu., Chesnokov S.S., et al. *Opt. Express*, **3**, 180 (1998).
16. Wattellier B., Fuchs J., Zou J.P., Chanteloup J.C., Bandulet H., Michel P., Labaune C., Depierreux S., Kudryashov A., Aleksandrov A. *J. Opt. Soc. Am. B*, **20**, 1632 (2003).
17. Kudryashov A.V., Samarkin V.V., Sheldakova Yu.V., Aleksandrov A.G. *Avtometriya*, **48**, 52 (2012).
18. Aleksandrov A.G., Zavalova V.E., Kudryashov A.V., Rukosuev A.L., Sheldakova Yu.V., Samarkin V.V., Romanov P.N. *Quantum Electron*., **40**, 321 (2010) [*Kvantovaya Elektron*., **40**, 321 (2010)].
19. https://kayacameras.com/product-category/jetcam-high-speed-cameras/.
20. https://www.theimagingsource.com/products/industrial-cameras/.
21. Taylor G.I. *Proc. Roy. Soc*., **164**, 476 (1938).
22. Fried D.L. *J. Opt. Soc. Am*., **56**, 1372 (1966).
23. Antoshkin L.V., Botygina N.N., Emaleev O.N. et al. *Atmos. Oceanic Opt*., **11**, 1046 (1998) [*Opt. Atmos. Okeana*, **11**, 1219 (1998)].
24. Volkov M.V., Bogachev V.A., Starikov F.A. *19th Inter. Conf. Laser Opt. (ICLO) 2020* (St. Petersburg, 2020, Techn. Program, WeR4-p12). DOI: 10.1109/ICLO48556.2020.9285761.
25. Fried D.L. *J. Opt. Soc. Am*., **67**, 370 (1977).
26. Volkov M.V., Bogachev V.A., Starikov F.A., et al. *Atmos. Oceanic Opt*., **34** (7), 10 (2021) [*Opt. Atmos. Okeana*, **34**, 547 (2021)].
27. Brigham E.O. *The Fast Fourier Transform and its Applications* (Englewood Cliffs, N.J.: Prentice-Hall, 1988).
28. Greenwood D.P., Fried D.L. *J. Opt. Soc. Am*., **66**, 193 (1976).
29. Greenwood D.P. *J. Opt. Soc. Am*., **67**, 390 (1977).
30. Hardy J.W. *Adaptive Optics for Astronomical Telescopes* (New York: Oxford Univ. Press, 1998).
31. Noll R.J. *J. Opt. Soc. Am*., **66** (3), 207 (1976).